Acta Acustica 2024, **8**, 73

https://doi.org/10.1051/aacus/2024059

Topical Issue – Virtual acoustics

Available online at:
https://acta-acustica.edpsciences.org

SCIENTIFIC ARTICLE OPEN ACCESS

Filter-based first- and higher-order diffraction modeling for geometrical acoustics

Christoph Kirsch* and Stephan D. Ewert

[1] Medizinische Physik and Cluster of Excellence Hearing4all, Carl von Ossietzky Universität Oldenburg, Ammerländer Heerstr. 114-118, 26129 Oldenburg, Germany

Received 1 February 2024, Accepted 2 September 2024

Abstract – Geometrical acoustics (GA) offers a high computational efficiency, as required for real-time renderings of complex acoustic environments with applications in, e.g., hearing research, architectural planning, and entertainment. However, the assumed ray-like sound propagation does not account for perceptually relevant effects of diffraction. In indoor environments, diffraction at finite objects and apertures such as tables, music stands, and doors is of interest for computationally efficient rendering. Outdoors, buildings and barriers are relevant. Here, we extend the recent physically-based universal diffraction filter approximation (UDFA) for GA to approximate spectral effects of higher-order diffraction and apply it to a flat finite object and a double edge. At low frequencies, such effects predominantly occur when sound is diffracted repeatedly at the edges of a finite object, and at high frequencies when sound is propagating around subsequent edges of, e.g., buildings or sound barriers. In contrast to existing methods, the suggested filter approaches and topology offer spatially smooth infinite impulse response implementation for modelling higher-order diffraction at flat objects for arbitrary geometrical arrangements. For double diffraction at a three-sided barrier, errors are considerably decreased in comparison to a state-of-the-art sequential approach. Both suggested methods are computationally highly efficient and scalable depending on the desired accuracy.

Keywords: Digital filters, Scattering, Virtual acoustics, Geometrical acoustics

1 Introduction

Virtual acoustic (VA) environments can be used to mimic the listening experience in particular real or imaginary indoor or outdoor environments, using (room) acoustics simulation. In this context, geometrical acoustics (GA) methods based on image sources are frequently used to model direct sound and early reflections, assuming ray-like propagation and specular reflections, resulting in a high degree of computational efficiency. One limitation of such GA methods is that the direct or specularly reflected sound field is discontinuous at the boundaries where the line of sight to the sound source or the geometrical reflection path disappears. Those discontinuities lead to abruptly appearing or disappearing sound sources in dynamic scenes, which can undermine the perceived perceptual plausibility of the VA environment. To obtain an overall continuous sound field at such geometric boundaries, and to account for perceptually relevant effects of diffraction, most prominently observed when the direct sound path becomes occluded, diffraction has to be considered and additional edge diffraction paths with modified spectral content are required [1–3].

Determining diffraction paths that may contain multiple diffraction and reflection nodes is a challenging computational task that can present a bottleneck for real-time acoustic simulations. Recently proposed techniques allow for the computationally-efficient search for edge diffraction paths in arbitrary geometries [4, 5]. Still, determining the spectrum of diffraction paths, and implementing the spectral shapes is associated with considerable computational cost. Keller [6] proposed a description of diffraction in the framework of geometrical optics with an asymptotic solution for infinite wedges, offering an easier-to-manage expression compared to previous (exact) solutions (e.g., Biot-Tolstoy [7]). Subsequently, other asymptotic solutions for infinite wedges were proposed, applicable to a wider range of geometrical configurations, and using varying numbers of diffraction terms: Pierce [8] used two and three terms, and Kouyoumjian and Pathak [9] used four terms in their uniform theory of diffraction (UTD). With the simplification proposed by [10], UTD is reduced in computational complexity such that applications in virtual acoustics become feasible (e.g., [5, 11–13]).

When applying the above solutions for infinite wedges to finite wedges to maintain computational simplicity, deviations occur for smaller geometric structures, as

*Corresponding author: christoph.kirsch@uol.de

reported e.g., by [5]. To reduce the perceptual impact of the errors introduced by the infinite wedge assumption they resort to only auralizing a single diffraction path. For more accurate acoustic modeling, finite wedge diffraction has to be considered. Medwin [14] adapted the previous time-domain solution of Biot-Tolstoy [7] to finite wedges. Svensson et al. [15] reformulated the expression proposed by Medwin [14], forming a line integral over secondary sources along the wedge. Their solution, referred to as Biot-Tolstoy-Medwin-Svensson (BTMS) in the following, is particularly convenient to apply for finite wedges and was also reformulated in the frequency domain [16]. One specific advantage of considering secondary sources along the wedge is that BTMS can also be used for the computation of higher-order (HO) diffraction [17], e.g., from repeated diffraction at different edges of an object. There, HO diffraction leads to spectral effects predominantly at low frequencies (e.g., [15, 18, 19]). For finite reflectors, a high-pass effect is observed (see also [19–21]).

The above mentioned diffraction solutions are either only valid for infinite edges (e.g., UTD) or computationally quite involved and thus not directly applicable for real-time VA environments (BTMS), particularly considering HO diffraction. HO diffraction is also relevant for propagation at multisided sound barriers (e.g., [8, 10, 22, 23]). In a VA context, a similar propagation occurs around subsequent corners of buildings or in, e.g., U-shaped rooms and corridors.

Efforts have been made to reduce the computational complexity of the implementation of edge diffraction in GA, using pre-computed recursive filters that are efficient at runtime [3] or simplifying the time-domain BTMS solution for finite wedges [24] for a finite impulse response implementation. With high computational efficiency and low-latency implementation in mind, filter-based diffraction solutions were proposed [25–27], offering a physically-based, computationally highly-efficient method to model diffraction from arbitrary infinite and finite wedges. Ewert [26] derived filter representations of the asymptotic solutions [8, 9] and an approximation of BTMS in both frequency and time domain, based on modified fractional-order transfer functions and the corresponding impulse response. Diffracted sound is parametrized by cutoff frequencies derived from the geometry at the edge. For time-domain processing in VA applications, using variable delay lines and time variant (recursive) filters, a specific further advantage of such a physics-based method in contrast to data-driven approaches, is that filter parameters naturally and systematically change for interactive source and receiver motion and that their (frame-based) re-calculation requires only a low number of operations. The universal diffraction filter approximation (UDFA; [27]) introduces simplifications for finite edges and proposes a recursive filter design. For infinite edges UDFA offers a performance benefit of a factor of approximately 2 re UTD (see [27]), however, the main advantage is the applicability of UDFA to finite wedges. Furthermore, it was demonstrated that diffraction by a flat, rectangular plate can be modelled by superimposing the four individually filtered edge paths. UDFA also offers a rigorously derived asymptotic filter approximation with a transition to unit gain at the GA boundaries, suited to replace heuristic blending approaches (e.g., [5, 13, 28]). Towards real-time diffraction modelling with a focus on spatially smooth sound rendering, Kirsch and Ewert [29] suggested a filter topology for UDFA.

Regarding spatial perception of diffracted sound and VA rendering, [30] demonstrated a shift of the perceived (apparent) sound source location by a flat plate, using impulse responses measured in an anechoic chamber. The effect was successfully modelled in comparison to the acoustic measurements by considering edge diffraction. It was also shown that HO diffraction has to be considered for matching the measurements. These findings demonstrate the strength of path and physically-based diffraction modelling for spatial rendering. Other approaches on a more "macroscopic" level have been suggested recently, attempting to efficiently approximate the most salient spectral effects of diffraction from finite objects with data-driven methods [31–34].

Taken together, for VA applications, modelling diffraction is important regarding two aspects: i) A continuous "smooth" sound field is relevant for perceptual plausibility (see also, e.g., [31]), when sound sources and/or receivers are moving in the virtual space. With the visibility-dependence of the GA direct sound and specular reflection paths, an accurate continuous sound field can only be achieved by integrating diffraction effects. Moreover, the sound "shadow" of small finite objects must correctly disappear at larger distances. For this, ii) modelling effects of HO diffraction is relevant. A model for "double" diffraction at two consecutive edges provides the prototype diffraction function for modelling paths around three-dimensional objects, e.g., buildings or consecutive corners in indoor environments.

In the VA context, HO diffraction at consecutive edges has so far commonly been simplified by considering a sequence of single-edge diffractions for constructed (virtual) source and receiver positions, (e.g., [12, 13, 28, 35]). These approaches can lead to considerable spectral errors and generally assume (far field) large spacing between edges. While, e.g., [28], provides a computationally-efficient sequential solution for double diffraction in the shadow of both edges, the transition to conditions where only one edge of a three-sided barrier casts a (sound) shadow, is disregarded. The effects of HO diffraction at finite objects have so far been most commonly considered in the context of backscattering from finite reflectors [18, 20, 21] and for loudspeaker enclosures (e.g., [36]). So far, there is a lack of physically-based approximations for higher-order and double diffraction for applications in VA and sound rendering, offering computationally efficient calculations and spatial smoothness of the rendered sound field.

Here, we extend UDFA [27, 29] to approximate HO diffraction in two example cases that are highly relevant for interactive acoustics simulations. The underlying filter topology for continuous sound field rendering is demonstrated for the square wedge (e.g., a building or room corner). For the first example case of a flat plate (e.g., a

table, door, or screen) it is demonstrated how a continuous sound field is achieved for arbitrary geometrical arrangements of source, receiver object, considering geometrical sound propagation, and first-order diffraction for each involved edge, and an additional filter approximation for effects of HO diffraction. Secondly, using the example of a three-sided barrier as a prototype for diffraction at two consecutive edges, a filter approximation is suggested to simplify the contribution of multiple diffraction terms from the two edges and higher-order combinations. For both example cases, we propose a highly-efficient infinite impulse response (IIR) filter architecture enabling smooth transitions of the approximated sound field across the GA shadow and reflection boundaries including a heuristic approximation of the spectral effects of HO diffraction from finite objects at low frequencies. The results are compared to the BTMS reference solution as available in the ED-Toolbox [37].

This paper is structured as follows: Section 2 outlines the basics of the singly-diffracted field at a wedge and UDFA. In Section 3, UDFA is extended: First, the basic filter topology for spatially smooth rendering using the example of first-order diffraction at a room corner is suggested. Second, the concept is expanded to flat (approximately two-dimensional) finite objects and the filter topology is extended to account for HO diffraction effects at low frequencies. Third, the filter solution is extended to cover double diffraction at three-sided barriers, providing the prototype for constructing diffraction around three-dimensional cube-like structures. Section 4 discusses and summarizes the results. The suggested modeling techniques are freely available as part of the UDFA toolbox [38].

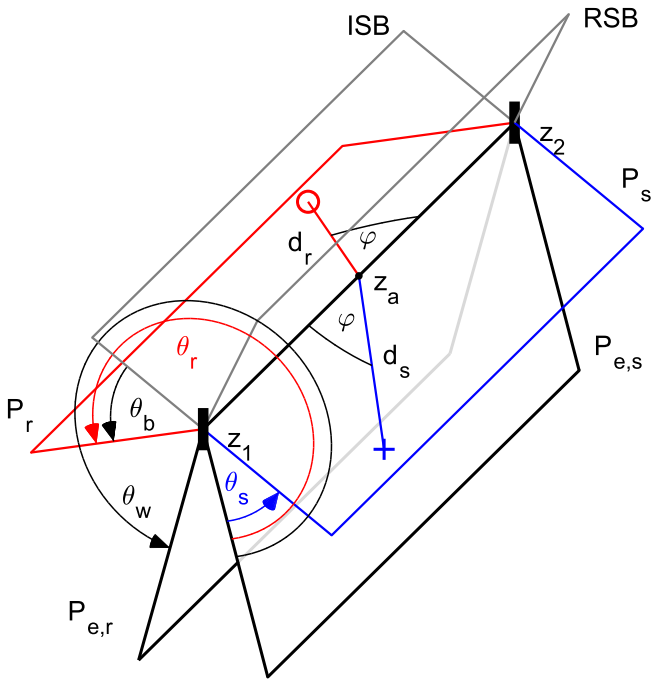

Figure 1. Two intersecting planes, $P_{e,s}$ and $P_{e,r}$, form a wedge located on the longitudinal z-axis of a cylindrical coordinate system, extending from z_1 to z_2, ($\pm\infty$ for an infinite wedge). Source (blue cross) and receiver (red circle) are located in the planes P_s and P_r (grey) at angles θ_s and θ_r, with all azimuth angles referenced to $P_{e,s}$. The shortest path between source and receiver intersects the edge at an angle φ at apex point z_a. The exterior wedge angle is referred to as θ_w. ISB and RSB denote the incident shadow and reflection shadow boundary, respectively.

2 Filter-based diffraction modeling

Here, we outline the underlying basics of the filter-based representation of the singly diffracted field at a wedge.

A rigid infinite or finite wedge along the z-axis of a cylindrical coordinate system is considered, formed by two intersecting planes as shown in Figure 1. The source (blue cross) is arbitrarily assumed to be closer to either wedge plane $P_{e,s}$ than the receiver (red circle), reflecting reciprocity of the problem. All azimuth angles θ are referenced to $P_{e,s}$. The receiver wedge plane $P_{e,r}$, is located at the exterior wedge angle θ_w. Source and receiver are located in the planes P_s and P_r with axial coordinates z_s, z_r, radial distances r_s, r_r, and azimuth angles θ_s, θ_r, respectively. At the apex point z_a, the incidence angle φ between edge and vector to the source in plane P_s equals the angle between edge and vector to the receiver in plane P_r. Past the incident shadow boundary (ISB) at $\theta_s + \pi$, the source becomes invisible to the receiver and only the diffracted field exists (referred to as shadow zone, SZ). In addition to the incident GA sound field in the "view" or "illuminated" zone (VZ), there is a reflected GA sound field in the reflection zone (RZ), separated by the reflection shadow boundary (RSB) at $\pi - \theta_s$ from the VZ. A diffracted transmission path between the source and receiver can be constructed using the apex point z_a on the edge, which serves as a center node. The distances between source and receiver and the apex point z_a are d_s and d_r, respectively.

Based on Ewert [26], UDFA [27] describes the diffracted sound by the superposition of a scalable number of one to four modified fractional-order low-pass filters. For general VA applications, using two terms is recommended, where the (infinite edge) cutoff frequencies for the low-pass filters are derived from the geometry at the wedge as [26, 27]:

$$f_{c\pm}(\theta) = \frac{2c}{\pi^2 d^* \sin^2(\varphi)} [N_\nu(\theta)]^2. \tag{1}$$

Here $d^* = 2d_s d_r / d$ is the characteristic distance and

$$N_{\nu\pm}(\theta) = \frac{\nu\sqrt{1 - \cos(\nu\pi)\cos(\nu\theta)}}{\cos(\nu\pi) - \cos(\nu\theta)}, \tag{2}$$

expresses the dependency of $f_{c\pm}$ on the source and receiver positions and the exterior wedge index $\nu = \pi/\theta_w$.

Filter gains are calculated as

$$g_{\nu\pm}(\theta) = \frac{\sin(\nu\pi)}{(1 - \cos(\nu\pi)\cos(\nu\theta))^{1/2}}. \tag{3}$$

Equations (1)–(3) are evaluated for $\theta_- = \theta_s - \theta_r$ and $\theta_+ = \theta_s + \theta_r$, resulting in two diffraction filters with the transfer function

$$H(f) = \left((jf/f_c)^{2/b} + (jf/Qf_c)^{1/b'} + 1 \right)^{-\alpha b/2}. \quad (4)$$

Here, $\alpha = 0.5$ is the fractional filter order and the parameters $b = 1.44$, $Q = 0.2$, and $r = 1.6$ have been determined to provide a smooth roll-off around the cutoff frequency [26]. For details on the filter-approximation of diffraction from finite wedges, see [27]. For further simplification, diffraction may be approximated by a single filter function. To match the asymptotic behavior at high-frequencies, the cutoff frequency can be calculated from the above two-term solution in equations (1)–(3) as shown in [27]

$$f_c(\theta) = \left(\frac{g_{v-}\sqrt{f_{c-}} + g_{v+}\sqrt{f_{c+}}}{2} \right)^2. \quad (5)$$

This single-filter approximation asymptotically approaches the physical reference at higher frequencies compared to the two-term approximation, particularly near the ISB and RSB, however, it offers reduced complexity and a smooth transition to GA direct sound when diffraction is only considered in the SZ (see also Sect. 3.1). For a more detailed theoretical description, see [26], and for the finite wedge approximation method and IIR implementation, see [27].

3 Extensions of filter-based diffraction modelling

To enable interactive real-time simulation of diffraction, we first introduce a filter topology ensuring continuous sound field modeling including the GA zone boundaries around diffracting objects with continuously changing recursive filters. Secondly, a flat plate composed of finite edges is considered, for which we propose a filter topology that results in spatial smoothness and approximates the spectral effects of HO diffraction. Finally, higher-order diffraction is considered in the context of a three-sided barrier. A filter-based approximation is proposed and compared to reference simulations as well as to a simpler sequential diffraction approach.

3.1 Filter topology for continuous zone transitions of the singly diffracted field

Figure 2 shows the transition between SZ and VZ at an infinite wedge with an exterior wedge angle $\theta_w = 270°$ as an example case, approximating a large scale building corner or also often used to approximate room corners. Figure 2d shows a projection of the radial plane (view in z-direction, along the edge), with the sound source position indicated by the blue cross and different receiver positions indicated by colored circles. The two left panels show the corresponding color-coded magnitude transfer functions for the BTMS reference (solid) and the suggested two-term filter solution (Fig. 2a, dashed) and single-term filter design (Fig. 2b, dotted). For calculating the BTMS reference for an infinite wedge, a wedge length of $d^* \times 100$ was used as an approximation. In the SZ (red traces), where only diffracted sound arrives at the receiver, all traces show a low-pass

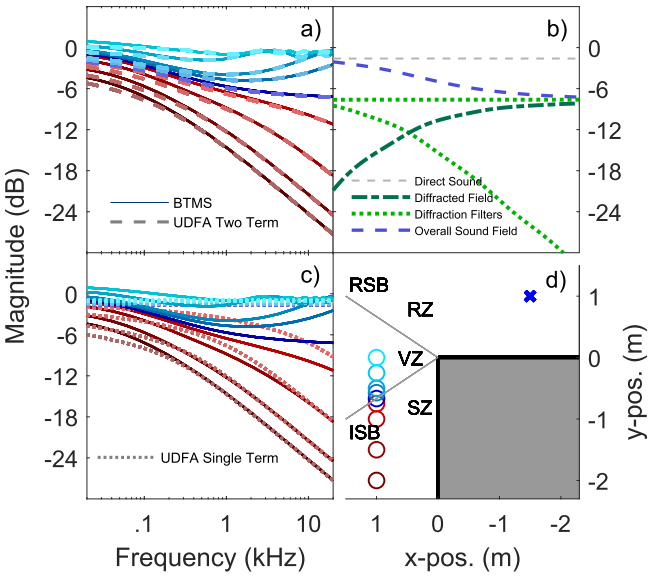

Figure 2. Magnitude transfer functions of the sound field at an infinite square wedge for different receiver positions indicated in panel d). The BTMS reference is shown as thin solid traces in panels a) and c). Panel a) and c) show the UDFA two-term and single-term approximation (colored, dashed and dotted traces), respectively. Panel d) shows the wedge (shaded, view in z-direction), the sound source (blue cross), and receiver locations (circles, color coded) matching a) and c). The incident shadow- and reflection shadow boundary (ISB, RSB) are indicated by thin grey lines, separating shadow zone (SZ), view zone (VZ), and reflection zone (RZ). The transition between SZ and VZ is shown in detail in panel b) for the UDFA two-term approximation. The blue, dashed trace is a replot from panel a) and shows the overall sound field at the ISB. The grey, dashed flat trace corresponds to the geometrical direct sound. The green, dotted traces correspond to the individual diffraction filters. The dark-green, dash-dotted trace is the sum of both diffraction components with the phase of one component inverted.

characteristic. The cutoff frequency rises with decreasing distance to the ISB. The slope of the filter is –3 dB/oct. At the ISB, the BTMS reference and two-term UDFA exhibit a lowpass shelving characteristic, while single-term UDFA shows a flat response with unit gain.

For BTMS and two-term UDFA (Fig. 2a), the sum of diffracted and direct sound in the VZ oscillates around the flat frequency response corresponding to the direct sound alone. This behavior is caused by the path difference between the geometrical direct sound and the diffracted sound. With increasing distance to the ISB, the amplitude of the ripples decreases as the sum of the diffracted components gets smaller (see also Fig. 2, [27]).

For an efficient real-time implementation of the two-term solution with recursive filters, we propose the topology illustrated in Figure 3. Direct sound and reflected sound are switched on and off, based on visibility tests, with GA distance attenuation and delay. Diffracted sound is implemented using the serial shelving filter design described in [27], and a separate phase-inversion stage at the output of each filter stage. Here, two parallel diffraction filters with the transfer functions $H_{\mathrm{diff},1}$ and $H_{\mathrm{diff},2}$ are used (two-term

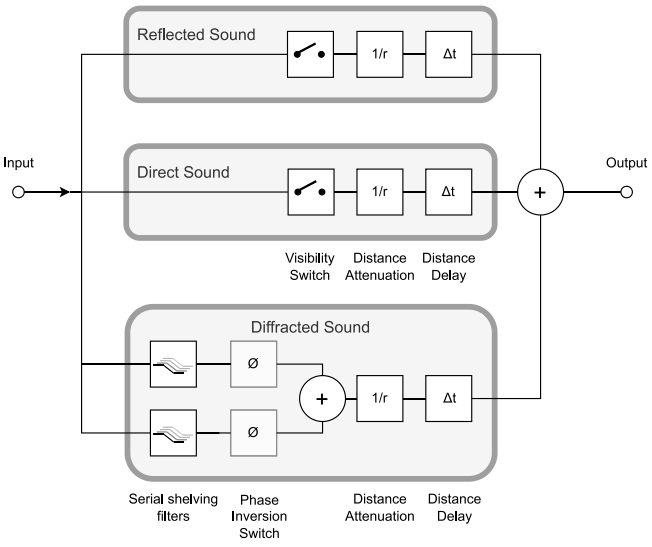

Figure 3. Block diagram for filter-based, spatially smooth diffraction auralization. In addition to direct and geometrically reflected sound, two diffraction filters are rendered, for which the output can be individually phase-inverted while retaining their IIR filter states.

solution from [27]). For increased accuracy, up to four of these filters can be used. The diffraction path length determines attenuation and delay.

Key to a "smooth" rendering is that the diffraction path is always present. At the ISB and RSB, the length of the diffracted path matches that of the direct or reflected sound path, respectively. For further illustration, the ISB transition is shown in Figure 2b. The dashed blue line is a replot from Figure 2a and shows the overall magnitude response at the ISB. The grey, dashed, horizontal trace indicates the GA direct sound component, which asymptotes the overall sound at low frequencies. The dotted green traces indicate the outputs of the two diffraction filters. The diffracted reflected sound shows a low-pass characteristic, whereas the diffracted incident sound shows a flat frequency response, given that the cutoff frequency for this component rises to infinity at the ISB (and the diffraction impulse response becomes a delta pulse, see also [26, 38, 39]). For this diffraction component, a polarity switch occurs at the ISB. The dashed-dotted trace in Figure 2b illustrates the sum of both diffraction components when they are out of phase. A smooth transition with this phase switch is achieved, given that

$$H_{\mathrm{dir}} - H_{\mathrm{diff},1} + H_{\mathrm{diff},2} = H_{\mathrm{diff},1} + H_{\mathrm{diff},2}, \tag{6}$$

with $H_{\mathrm{diff},1} = H_{\mathrm{dir}}/2$ at the ISB where $f_{\mathrm{c},1} = \infty$ and $g_1 = 1/2$, according to equations (1) and (3). In Figure 2b, the sum of both diffraction components (green, dotted) in phase is shown as the blue-dashed line representing the overall sound field within the SZ infinitely close to the ISB. Just beyond the ISB, in the VZ, the identical overall sound field arises when both components are out of phase (green, dash-dotted) and are superimposed with the geometrical direct sound (grey, dashed).

At the RSB, the same behavior as in equation (6) is observed for the diffracted reflected component with $f_{\mathrm{c},2} = \infty$ and $g_2 = 1/2$. At positions other than the zone boundaries, the sound field is continuous since the functions that define the parameters (Eqs. (1) and (3)) are smooth.

A smooth transition at the ISB can alternatively be achieved using a single diffraction filter with larger deviations from the real sound field, particularly outside the SZ and close to the ISB. In this case, a transition to unit gain at the ISB is desirable (e.g., [13]) and continuity of the overall sound field is not considered at the RSB. The single-term filter design of UDFA (see Eq. (5)), is indicated by the dotted line in Figure 2c. It is obvious that the error of this solution increases towards the ISB, where the single-term solution converges against a flat response, unlike the shelving behavior observed for the BTMS reference. The filter topology in Figure 3 has to be adapted and the single diffraction filter is switched off at the zone transition where the direct sound component is switched on. The inaccuracies of the single term solution might be less relevant if it is used for higher-order diffraction contributions. It should be noted that this single-term solution is suited to replace earlier approaches which "blend and fade" UTD to a flat response at the ISB, see, e.g., [13, 28].

3.2 Flat plate

We assume that flat objects such as tables, doors, and music stands can be approximated by an idealized two-dimensional, rigid plate, composed of several finite edges for which diffraction is modelled using UDFA. For a comparison between measurements of a real plate and UDFA, see [27] or [30].

In order to approximate the spectral effects of HO diffraction and to ensure a smooth sound field around the object, we propose the rendering architecture illustrated in Figure 4. The sound is split by a set of complementary high- and low-pass filters. The low-pass part is always rendered, regardless of visibility, as expected for wavelengths larger than the object. The path length either corresponds to the GA direct sound or, if occluded, to the shortest diffraction path. The high-pass part is rendered as described in Section 3.1, with direct and reflected sound, and a separate diffraction path for each edge of the object. When the source is visible, the complementary cross-over filters result in a flat response for the direct sound component. While in [29], first-order filters were originally suggested for simplicity, the spectral accuracy can be improved by using 2nd-order Linkwitz-Riley filters.

As suggested in [27], the cross-over frequency for the two complementary filters is based on Rindel [20, 21], who proposed a limiting frequency f_{g} for rectangular reflectors, above which diffraction losses at a reflector "can be considered negligible":

$$f_{\mathrm{g}} = \frac{cd^*}{2S\cos(\gamma)}, \tag{7}$$

where d^* is the characteristic distance to the reflection point, S is the surface area of the reflector and γ is the

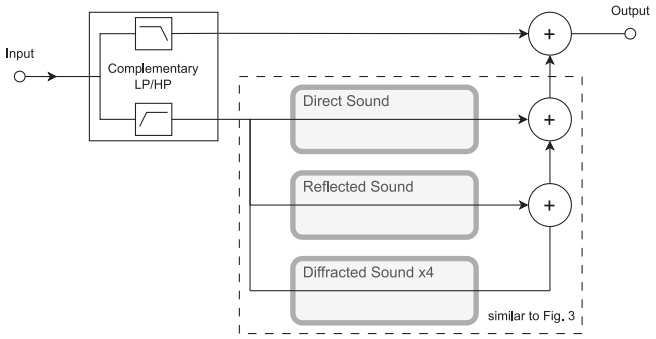

Figure 4. Extended rendering architecture for a spatially smooth sound field around a finite flat object, based on the block diagram shown in Figure 3.

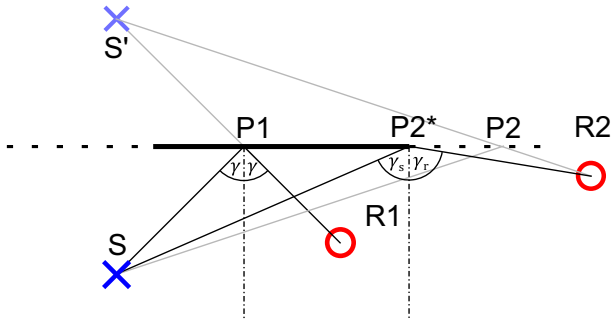

Figure 5. Birdseye view of flat plate (solid black bar), with sound source S (blue cross), image source S' (faint blue cross) and two receiver positions R1 and R2 (red circles). Paths between (image) source and receivers are shown via the geometrical reflection points P1 and P2 (virtual, outside the physical plate), and the reflection point P2* constrained to the plate. The angle γ between the reflection paths and the plate normal are shown for P1 and P2*.

angle between the plate normal and the geometrical reflection on the plate (or extension thereof). Given that first-order diffraction is already accounted for by UDFA, covering the slope of the high-pass filter in the diffraction function around f_g, $f_g/2$ appears to be a good choice as resulting cross-over frequency, supported by inspection of the combined effect of UDFA and the additional cross-over filter structure in Figure 6f, where for position 7 and 8, the dotted traces closely match the (solid) reference at low frequencies.

To achieve a smooth sound field, we propose a modification to the definition of γ. In Figure 5, the geometrical reflection from the sound source S (blue cross) to the receiver R1 (red circle) occurs at the point P1 located on the surface of the plate (shown as a black bar in the two-dimensional projection, view from within the plate plane). Here, γ is the angle between the reflection path and the plate normal, as defined by [20, 21]. If the GA reflection disappears and the virtual reflection point is located outside of the plate, as it is the case for P2 in Figure 5, the point from which γ is calculated is constrained to be within the plate. In such cases, there are two different angles γ_s and γ_r for the source and receiver, respectively. The larger angle is used in equation (7), resulting in $f_g \to \infty$ when source or receiver are located in the plate plane (dashed horizontal line in Fig. 5). With $f_g \to \infty$, the diffracted sound is faded out as the plate plane is approached, resulting in a smooth transition that would not be possible without constraining the reflection (or intersection) point to the plate, since γ would not reach 90°. If sound source and receiver are located on opposite sides of the plate, γ is calculated as the angle between the plate normal on either side and the path connecting source and receiver, with the intersection point of the object plane again constrained to the plate. Depending on the object size and the geometrical arrangement, the diffracted and reflected sound are high-pass filtered, reducing errors at low frequencies, most notably for objects acting as finite reflectors.

Figure 6 shows the magnitude transfer functions for different sound source positions indicated by crosses in the top panel. In the left column, first-order diffraction is considered for both the BTMS reference (thin, solid) and UDFA (dashed). Additionally, the faint thick traces in Figure 6a show the results for UTD, ignoring the finite length of the edges of which the plate is comprised. In the right column, HO-BTMS (15th order) and UDFA with the proposed architecture are shown.

Figures 6a and 6b show the overall sound field for source positions 1–3 on the plate side opposite to the receiver (red circle). At position 1, the sound source is centered behind the plate, and the four diffraction paths are identical. The reference exhibits spectral ripples, which are not represented by UDFA. First- and HO diffraction differ at low frequencies, where HO diffraction results in a low-shelving characteristic. Position 2 is located at the ISB, where a transition occurs that is conceptually similar to the one described in Section 3.1. Spectral ripples in the reference at high frequencies are reproduced by UDFA, given that they are mainly caused by path differences of the contributions from the individual edges. As expected, considerable errors occur for UTD at position 1 where only diffracted sound reaches the receiver and become less severe as the receiver transitions to the view zone at positions 2 and 3[1]. In Figure 6b, the effect of HO diffraction is reproduced by UDFA, matching the reference at very low frequencies. However, the proposed architecture may introduce deviations due to path differences between the diffraction paths and the low-pass component, e.g., for position 2 at around 125 Hz.

Figures 6c and 6d show the response for sound sources located very close to either side of the plate-plane (position 4 and 5). Because position 5 is located closer to the receiver

[1] For the UTD traces shown here, the contributions from those edges with an apex point outside the physical edge were switched off. This reduces the spectral error shown, however, leads to a discontinuity in the transition from positions in which four edges have an apex point on the edge towards positions in which there are only two edges with physical apex points. According to the above paradigm, there are also spatial conditions which no diffracted sound would be rendered, leading to very prominent discontinuities in the sound field. Such problems can be avoided with UDFA and its extensions presented here.

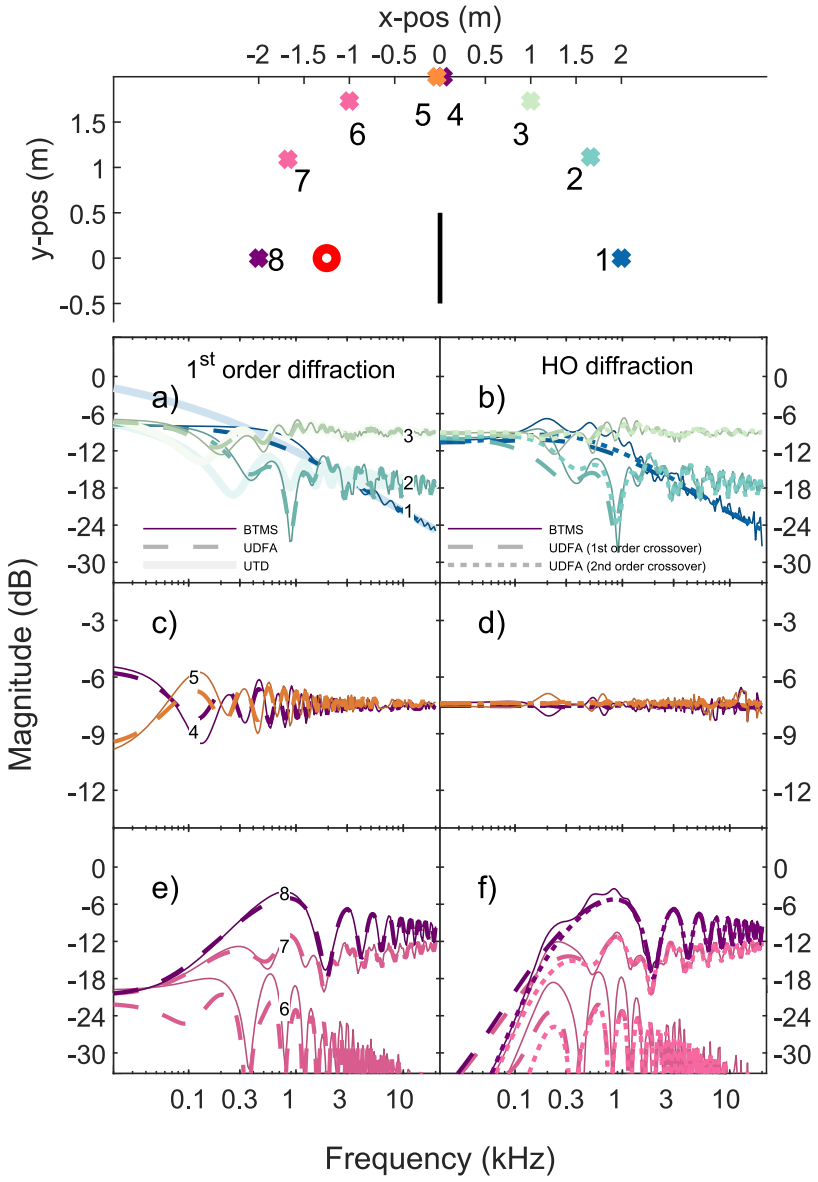

Figure 6. Transfer functions for different source positions near a plate. Top panel: geometrical arrangement of the plate (black line, view from above in the plate plane). The receiver is indicated as red circle and sound source positions are indicated by colored crosses. Left column: first-order diffraction, BTMS (thin, solid) and UDFA (dashed). Right column: HO-BTMS (15th order) and UDFA with the architecture according to Figure 5, with 1st-order (dashed) and 2nd-order (dotted) crossover. Note that the y-axis scale is magnified in panels c) and d) for improved clarity.

than position 4, there is a frequency-independent level difference. When only first-order diffraction is considered in Figure 6c, a phase switch of the ripples is observed for BTMS and UDFA, causing a discontinuity for the plate-plane transition. This is caused by a direct transition from SZ to RZ for the edges of the idealized flat object. The HO-BTMS reference in Figure 6d exhibits considerably smaller ripples compared to first-order diffraction, especially at low frequencies. The HO response is reproduced by UDFA with the proposed cross-over filters, for which f_g converges towards infinity as sound source or receiver approach the plate-plane. Consequently, the high-pass part containing spectral ripples caused by the superposition of diffracted and direct sound disappears, and a flat frequency response is rendered below the infinite crossover frequency f_g. It should be noted that the same completely flat response would also be expected for the reference solution for an infinitely thin plate, when even more HO terms are included.

The source positions in Figures 6e and 6f are mirrored versions of those in Figures 6a and 6b. For clarity, the direct sound is disregarded in the transfer function plots. For position 6, no geometrical reflection is present, and a -3 dB/oct envelope low-pass behavior is observed at high frequencies. Position 7 is located at the RSB. The corresponding transfer functions are attenuated by about 6 dB in the mid frequencies and converge to those of position 8 at high

frequencies. The geometrical reflection point is at the center of the plate for position 8. The transfer functions oscillate around a flat frequency response at high frequencies. As previously described in [18, 19, 27], first-order diffraction (Fig. 6e), leads to a low-frequency shelving characteristic, whereas, for HO diffraction (Fig. 6f), a high-pass characteristic is observed. The high-pass slope for HO-BTMS is steeper (approx. 12 dB/Oct) than that of the proposed UDFA 1st-order crossover filter (dashed). With the 2nd-order filter (dotted), the correct behavior is matched at the computational expense of the higher filter order. Differences between the 1st- and the 2nd-order crossover filters are mainly visible in Figure 6f and less pronounced otherwise.

3.3 Three-sided wedge

Repeated diffraction at multiple corners occurs frequently for three-dimensional objects, e.g., for double-diffracted paths around a cube (approximating a building) or the three-sided sound barriers with finite width. Indoors, a double corner is a prominent example. Approximate solutions for infinite three-sided wedges with finite width have been suggested in [8] with expansions in [22]. Kawai [10] provided high-frequency approximations for multisided barriers showing good agreement with measurements. However, even with neglecting high-order diffraction terms beyond the second order, Kawai's solution would result in four diffraction functions (two first- and two second-order) per double edge. Moreover, for thin barriers, diffraction orders higher than two become increasingly relevant. Based on the concepts described by Pierce [8] and Kawai [10], we suggest further simplifications to reduce the number of terms and to approximate HO diffraction.

3.3.1 Proposed approximation

We approximate diffraction at double corners by two cascaded diffraction filters for each of the two edges. In the "single shadow zone" where only one edge occludes the source or receiver, one of the cascaded filters is muted with smooth transitions of the mixing coefficients at the zone boundaries. By this, the required transitions between the asymptotic −3 dB/oct slope for first-order diffraction and −6 dB/oct for double diffraction can be achieved.

Figure 7 shows the geometry of the double edge, defined by two exterior wedge angles $\theta_{w1,2}$ and the finite width d_w. Depending on the width of the edge, we introduce the modified exterior wedges angles

$$\hat{\theta}_{w1,2} = \theta_{w1,2} + \frac{\beta\, d_{1,2}^2}{d_w + d_{1,2}^2}(\theta_{w2,1} - \pi), \tag{8}$$

assuring a transition to the knife edge case for $d_w = 0$. Here $d_{1,2} = d_{s1,2} + d_{r1,2}$ are the diffracted path distances across either wedge, potentially intersecting the double edge. The factor $\beta(\theta_{r1,s2})$ is typically 1 and linearly transitions to 0 for single diffraction at either edge in the range $(\theta_{w1} > \theta_{r1} > \theta_{w1} - \pi/6, \theta_{w2} < \theta_{s1} < \theta_{w2} + \pi/6)$. To account for single diffraction, two diffraction filters, $D_{1,2}$ (UDFA, two-term solution) are derived for either edge using the

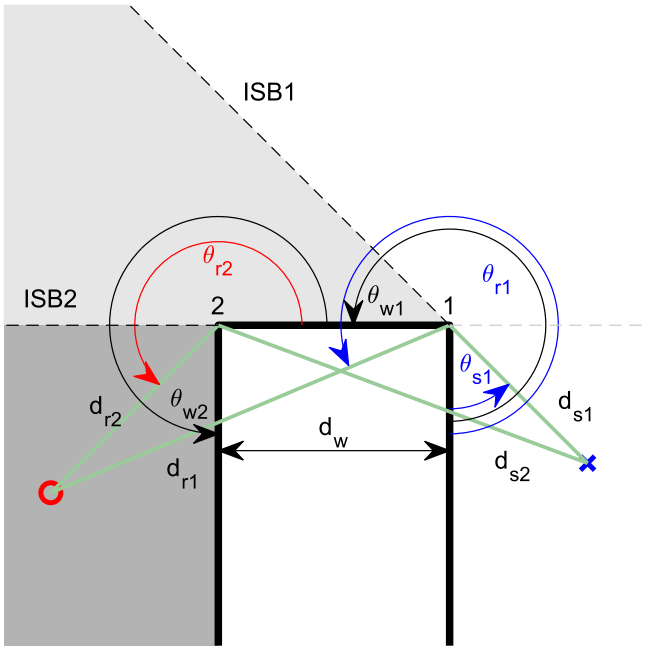

Figure 7. 2D projection of the double edge with exterior wedge angles $\theta_{w1,2}$ and finite width d_w, extending the geometry of the single wedge in Figure 1. The source (blue cross) and receiver (red circle) are arbitrarily assigned to one of the edges and are located at the distances d_{s1} and d_{r2} at angles θ_{s1} and θ_{r2} with respect to edge 1 and 2 respectively, so that $\theta_{s1} < \theta_{r1}$ The light grey area shows the "single" SZ and the dark grey area the "double" SZ.

distances $d_{s1,r2}$ and $d_{r1,s2}$ or the "detour" distance $d_w' + d_{r2,s1}$ in the double diffracted case (as depicted in Fig. 7):

$$D_{1,2} = D\Big(d_{s1,r2},\, d_{r1,s2}|(d_w' + d_{r2,s1}),\, \theta_{s1,r2}, \theta_{r1,s2}, \varphi,\, \hat{\theta}_{w1,2}\Big). \tag{9}$$

Here d_w' denotes the distance across the top of the double edge, considering the incidence angle φ (see Fig. 1). For $\varphi = \pi/2$, d_w' equals d_w. For the current notation, it is assumed that $\theta_{s1} < \theta_{r1}$, otherwise the assignment of source and receiver is reversed. To account for double diffraction, two further simplified diffraction filters are constructed to mimic the contribution of the second edge, limited to conditions with the receiver in the "double shadow zone" (dark grey area in Fig. 7). For this, the single-term filter (Eq. (5)) is used, which transitions to unit gain in the view zone of the (second) edge:

$$D_{12,21} = D(d_{w',s1},\, d_{2,w'},\, \theta_{0,s1}, \theta_{r2,w}, \varphi,\, \theta_{w2,1}). \tag{10}$$

This filter uses the (unmodified) wedge angles $\theta_{w2,1}$ of the other edge and the distance d_w' across the top of the double edge to the apex point on the first edge (instead of taking the distance to the opposed receiver or source). The overall diffracted field is composed of the contributions from both edges, expressed as

$$D = (1 - \alpha)D_1 D_{12} + \alpha D_2 D_{21}, \tag{11}$$

with the weighting factor

$$\alpha = \begin{cases} 1-\alpha_{12} \text{ in VZ} \\ \alpha_{12} \text{ otherwise} \end{cases}, \quad \alpha_{12} = \frac{1}{\frac{f_{c12}}{f_{c21}}+1}. \tag{12}$$

Here, the cutoff frequencies $f_{c12,21}$ are for the corresponding diffraction filter transfer functions $H_{12,21}$ (see Sect. 2) representing diffraction functions $D_{12,21}$, respectively.

The contribution of the diffraction functions in equation (11) depends on the zones in which source and receiver are located: In the "double" SZ where the receiver is located in the SZ of both edges (with the direct path between source and receiver intersecting both wedges; dark grey area in Fig. 7) there are two double diffracted contributions with α ranging from 0 to 1. Reciprocity is ensured by including both edge contributions. While both terms obey reciprocity, they are not identical for asymmetric conditions ($\alpha \neq 1/2$). Thus, using only the first or second term for further simplification would still ensure reciprocity, however, the resulting approximation would show slight differences. In the double SZ, $D_{1,2}$ are based on the modified exterior wedge angles $\hat{\theta}_{w1,2}$ with $\beta = 1$. At the extension plane of the top of the double edge, the ISB of $D_{12,21}$ is located, resulting in $f_{c12,21} = \infty$ (see ISB2 in Fig. 7). Accordingly, here, one of the terms in equation (11) disappears.

In the "single" SZ (light grey area in Fig. 7), one shadowing edge dominates the overall diffraction function at high frequencies. In equation (11), the weighting factor α becomes either one or zero, and the second-order term $D_{12,21}$ of the opposite edge shows a flat response with unit gain (given that either $f_{c12,21} = \infty$). In the single SZ of edge 1, equation (11) thus reduces to $D = D_1$ with modified exterior wedge angle $\hat{\theta}_{w1}$ and respectively so for edge 2. The effect of the second edge at low frequencies is accounted for in the modified exterior wedge angle $\hat{\theta}_{w1,2}$, predominantly for small d_w and for either source of receiver located closely above the plane extending the top of the double edge. The high-frequency effect of the second edge disappears at angles above top plane for $\theta_{r1} > \theta_{w1} - \pi/6$, $\theta_{s2} < \theta_{w2} + \pi/6$, where $\beta(\theta_{r1,s2}) = 0$ and $\hat{\theta}_{w1,2} = \theta_{w1,2}$, accordingly. The low-frequency effect of the second edge persists and is accounted for by lowering the (DC) gain, and by accordingly transforming the cut off frequencies of the diffraction filters (see Appendix) to maintain the high-frequency response. Given the reciprocity of the single wedge solution, reciprocity is ensured here. Likewise, in the "single" VZ (white area on the right-hand side of Figure 7, below the dashed grey horizontal line), the singly diffracted field from one edge is considered, here $D = D_1$.

In the "double" VZ (with both source and receiver above the top plane of the double edge, where each can "see" both edges), two singly diffracted fields from both edges are considered. Here both second-order terms show unit gain and equation (11) reduces to $D = (1-\alpha)D_1 + \alpha D_2$.

At the expense of precision in the single SZ and VZ, $\beta = 1$ may be chosen for all angles, simplifying the filter parameter calculations. Concurrently, the connected low-frequency gain compensation (Appendix) is not required. Alternatively, the low-frequency gain compensation might also be applied in the double SZ for further improvements.

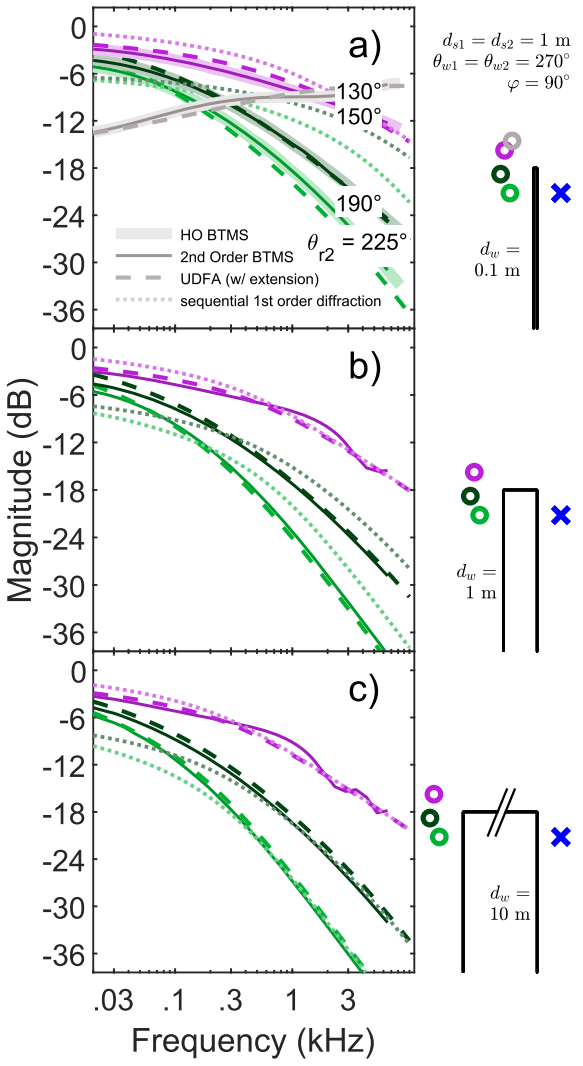

Figure 8. Magnitude transfer functions for infinite double edges with a systematic change of receiver angle θ_{r2}. The geometry is sketched on the right, with the blue cross indicating the source position and the colored circles indicating the receivers to which the traces in the left column correspond. θ_{s1} is 45° for all traces. Each row corresponds to a different value for d_w, with 0.1 m, 1 m, and 10 m from top to bottom. The 10th-order BTMS reference is shown as thick, faint solid traces, and 2nd-order BTMS is shown as thin solid traces. The filter-based approximation according to equation (11) is shown as dashed traces. The dotted traces show the results for sequential diffraction filtering. The results are normalized to the shortest unobstructed distance from source to receiver.

3.3.2 Qualitative evaluation

The results of the above-described approximation are depicted as dashed traces in Figures 8 and 9, with the solid traces indicating the BTMS reference that has been simulated up to the 2nd diffraction order. Simulating higher diffraction orders has only little effect on the resulting transfer function, while drastically increasing the computation time. Simulations up to the 10th-order diffraction are shown as faint traces in the background in Figure 8a.

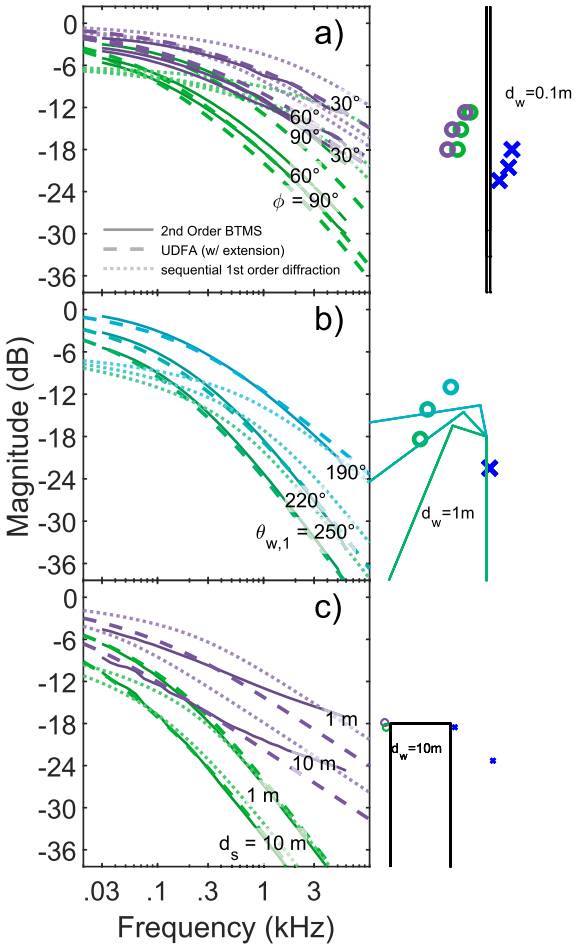

Figure 9. Magnitude transfer functions for infinite double edges with example variations of different parameters (see geometry sketches on the right). Unless stated otherwise: $\theta_{w1,2} = 90°$, and θ_{s1} is 45°. In panel a), the incidence angle φ is varied for two $\theta_{r2} = 170°$ (dark purple) and $\theta_{r2} = 225°$ (green), in panel b), the wedge angle θ_{w1} is varied for a fixed $\theta_{r2} = 225°$, and in panel c) the distance of the source d_{s1} is varied for $\theta_{r2} = 170°$ (dark purple) and $\theta_{r2} = 225°$ (green).

The additional dotted lines show the results for sequential diffraction filtering as suggested in, e.g., [28] for the double SZ. Unless stated otherwise, $\theta_{w1,2}$ was 90° as depicted in Figure 7, the source and receiver distances were 1 m, and the source was located at θ_{s1} of 45°. The three rows are for d_w of 0.1 m, 1 m, and 10 m, from top to bottom. In Figure 8, the receiver angle θ_{r2} was systematically varied (consistently color-coded across all panels). In the right column, the geometrical arrangements are depicted using the same color coding for the receiver (circles) as for the respective traces in the left column. Both the reference and the proposed approximation exhibit a low pass behavior in the single SZ (SSZ) and double SZ (DSZ) and a high-pass behavior in the single VZ (grey trace in Fig. 8a). Systematic deviations between approximation and reference occur predominantly at low frequencies (up to about 1–1.5 dB at 30 Hz), related to the asymptotic behavior of the two-term and single-term solutions used here. In the double shadow zone, e.g., for $\theta_{r2} = 225°$, shown as light green traces, a −6 dB/oct slope is observed at high frequencies. Here, the maximum deviation between the approximation and the reference of about 2 dB at 3 kHz and above is observed for the smallest edge width d_w of 0.1 m in Figure 8a. The slope flattens for smaller receiver angles (see $\theta_{r2} = 170°$, dark green traces), whereas in the single shadow zone ($\theta_{r2} = 150°$, purple), the diffraction functions asymptote to –3 dB/oct as would be expected for the singly diffracted field. The ripples observed in the BTMS reference, originating from a superposition of contributions from both edges (at different delays) are not reproduced by the approximation suggested here, which simplifies to the singly-diffracted field of edge 1 in this case. This leads to frequency-dependent deviations between the approximation and the reference with a maximum of about 2 dB at 2 kHz in Figure 8b. Figure 8c shows the case in which d_{s1} and d_{r2} are small compared to $d_w = 10$ m. Here, deviations between approximation and reference mainly occur at 1 kHz (about 2 dB) in the single SZ (purple trace) and when entering the double SZ (dark green trace, about 1 dB for all frequencies). At this large edge width, the high-frequency behavior in the DSZ is matched by the sequential approach (dotted), which deviates systematically at low frequencies (up to about 4–5 dB at 30 Hz). As can be expected, the high-frequency error of the sequential approach increases the smaller the edge width, see Figure 8a, with a maximum deviation of up to 12 dB at 3 kHz and above. In the single SZ, where one of the diffraction filters of the sequential approach shows unit gain, deviations from the reference are observed, which without modifying the filter gain would be further increased by 6 dB, which will be discussed later.

In Figure 9 several other parameters of the edge geometry were altered as an example for the same three edge widths as in Figure 8. Again, the right panel depicts the geometrical arrangements. As observed in Figure 9a, a shallower incidence angle φ (see also Fig. 1) leads to increased low-pass cutoff frequencies in both the double and single SZ. The largest error of the current approximation is observed at high frequencies (up to about 3 dB). The sequential approach (dotted traces) also shows a varying cutoff frequency depending on the incidence angle, but similar to the scenarios shown in Figure 8a, there are large errors (up to 12 dB at high frequencies) due to the narrow width of the edge. In Figure 9b, the variation of the exterior wedge angle θ_{w1} from the square wedge towards a nearly flat plane (at $\theta_{w1} = 190°$) for the receiver in the double SZ, resulting in a transition from a from a −6 dB/oct slope towards a −3 dB/oct slope typical for diffraction at the single (remaining) edge. While the here proposed approximation (dashed) closely matches the reference with the largest deviation of about 2 dB at 5 kHz for $\theta_{w1} = 190°$, the sequential approach leads to considerable errors at low frequencies (up to about 7 dB for $\theta_{w1} = 190°$), and at high frequencies, particularly for large θ_{w1} (up to about 6 dB). In Figure 9c, the effect of increasing d_{s2} is closely approximated in the double SZ (green traces) by the proposed approximation with a maximum error of about

1 dB at 3 kHz. Here, the sequential approach performs well at high frequencies but again deviates from the reference at low frequencies (up to 5 dB at 30 Hz). In the single SZ, the proposed approximation matches the reference at low frequencies but diverges towards high frequencies, reaching an error of about 4–5 dB at 5 kHz. The reason for this mismatch is that at low frequencies, the modification of the exterior wedge angles (Eq. (8)) is appropriate while at high frequencies the width $d_w = 10$ m of the double edge "appears to be infinite" with respect to the wavelength. Accordingly, the exterior wedge angle modification should not be applied. For smaller angles θ_{r2}, see purple trace in Figure 8c, the factor β accounts for this, and fades out the modification, however, so far independent of d_w. Improvements could be achieved here by further optimizing the geometry dependency of factor β or by blending between the here suggested solution with modified exterior angle and the sequential approach using a d_w-dependent cross-over frequency. While the sequential approach performs considerably worse than the current approach up to 1 kHz, it better asymptotes the reference at very high frequencies, with a frequency-independent error of about 3–4 dB above 100 Hz.

3.3.3 Quantitative error evaluation

Randomized geometries were generated in order to quantify the error of the proposed approximation. Since differences between 2nd-order and high-order BTMS are generally small for double wedges in the SSZ and DSZ (observed in Fig. 8a and also described in [22]), 2nd-order BTMS served as a reference. Magnitude transfer functions were calculated for the tested geometries at a perceptually motivated third-octave scale with 23 center frequencies ranging from 50 Hz to 8 kHz. Similar to Figures 8 and 9, the transfer functions were normalized to the shortest free travel distance. In addition, the proposed approximation was also compared to the sequential diffraction filtering in the DSZ and to a single diffraction filter in the SSZ (as also shown in Fig. 8 and 9, dotted lines). It should be noted that for this sequential method, additional modifications would be required for a smooth transition from SSZ to DSZ. Currently, in the DSZ, a gain of 0.5 is applied to the sequential filters (see also [23, 28]), while no gain is applied to the single filter in the SSZ. A smooth transition could be achieved by also applying the same gain in the SSZ, however, at the cost of considerably increased errors (including a discontinuity at the remaining ISB).

Sets of 1000 geometries were generated for the three different barrier widths $d_w = 0.1$ m, 1 m, 10 m, for square wedges ($\theta_{w1} = \theta_{w2} = 270°$), and for wedges with θ_{w2} drawn from a uniform distribution between 210° and 270°. The other parameters were drawn from uniform distributions as shown in Table 1. For each dataset, cases were drawn until 500 geometries in each the SSZ and the DSZ were generated. Geometries in the VZ were rejected. To avoid numerical problems when generating the BTMS reference data, geometries with sources or receivers located within 1.5° of ISB1 or the extensions of the wedge planes were rejected.

Table 1. Parameter ranges for error evaluation.

Parameter	Min. value	Max. value
θ_{s1}	0°	90°
θ_{r2}	0°	270°
d_s	0.5 m	4.0 m
d_r	0.5 m	4.0 m
φ	30°	90°

Table 2 shows the resulting average Root-Mean-Square-Error (RMSE), and the 5% and 95% percentiles, calculated based on the dB-differences between the BTMS reference and the evaluated approximations. Additionally, the average relative error is provided, indicating the average absolute dB deviation of the magnitude transfer functions. The reference RMS energy values give an indication as to how much energy is transmitted into the tested regions, thus hinting at the perceptual relevance of the diffracted sound. As expected, more energy is transmitted into the SSZ (approx. −7 dB) compared to the DSZ (−16 dB to −10 dB).

Compared to the 2nd-order BTMS reference, the proposed extension of UDFA results in small average relative errors in the DSZ (<0.87 dB) and slightly larger errors in the SSZ (0.70–1.22 dB), where values larger than 1 dB occur for $d_w = 1$ m and $d_w = 10$ m. Error values show similar trends regardless of θ_{w2}, with a tendency of slightly increased errors for $\theta_{w2} = 270°$. Such errors of approximately 1 dB can be considered perceptually small [41–43] based on psychoacoustic experiments involving spectral differences.

The further simplified sequential diffraction model in the DSZ and a single edge in the SSZ lead to larger average relative errors than the proposed approximation in all tested geometry sets. Furthermore, RMSE results are distributed in a broader range (as indicated by the values for the 5% and 95% percentiles) for the sequential diffraction. As can be expected for wide barriers ($d_w = 10$ m) with large spatial separation of the two wedges, the assumptions for a purely sequential or single-wedge representation of double diffraction are best met, and the best results are observed in the SSZ for the single diffraction filter with an average relative error of 0.97 dB, performing only slightly worse than the proposed approximation (0.89 dB). In all other tested geometries, the sequential/single diffraction approach performs consistently worse (with considerably larger relative absolute errors up to 5 dB) than the proposed approximation. Also, as can be expected, the largest errors (5 dB) for the sequential approach occur for the smallest edge width, $d_w = 0.1$ m, where the proposed approximation shows an error of 0.87 dB.

4 Computational complexity

A runtime evaluation for the underlying UDFA approach was presented in [27], where the computation time for 30,000 geometrical configurations was tested in a loop without vectorization of the underlying operations.

Table 2. Error measured for the proposed extension to UDFA and for sequential diffraction (in parentheses) re 2nd-order BTMS. All results are shown in dB. Bold values indicate the average relative error.

		$d_w = 0.1$ m		$d_w = 1$ m		$d_w = 10$ m	
		SSZ	DSZ	SSZ	DSZ	SSZ	DSZ
$\theta_{w1} = \theta_{w2} = 270°$	RMS (ref.)	−7.36	−12.2	−7.00	−13.6	−6.88	−16.1
	RMSE 5% percentile	−35.1 (−29.9)	−41.9 (−24.1)	−32.1 (−30.8)	−46.1 (−28.4)	−31.5 (−30.9)	−55.0 (−36.1)
	RMSE average	−27.8 (−19.3)	−36.7 (−21.3)	−24.6 (−19.9)	−38.7 (−24.6)	−22.0 (−22.7)	−43.2 (−29.0)
	RMSE 95% percentile	−22.4 (−10.4)	−31.7 (−17.8)	−13.8 (−2.14)	−31.7 (−20.0)	−13.9 (−15.2)	−30.2 (−22.3)
	Avg. rel. error	**0.82 (2.24)**	**0.87 (5.0)**	**1.22 (2.70)**	**0.71 (2.42)**	**1.16 (1.22)**	**0.64 (1.07)**
$\theta_{w1} = 270° \; \theta_{w2} = 210°...270°$	RMS (ref.)	−6.77	−10.6	−6.59	−12.1	−6.85	−13.5
	RMSE 5% percentile	−36.2 (−34.2)	−44.4 (−23.1)	−33.6 (−33.2)	−47.6 (−28.2)	−32.6 (−32.7)	−51.7 (−32.1)
	RMSE average	−28.9 (−22.1)	−36.7 (−18.8)	−26.0 (−21.2)	−37.4 (−20.1)	−24.0 (−24.0)	−40.5 (−24.2)
	RMSE 95% percentile	−21.5 (−11.7)	−30.3 (−14.0)	−13.4 (−1.95)	−29.9 (−14.0)	−15.5 (−16.9)	−29.6 (−16.6)
	Avg. rel. error	**0.74 (1.77)**	**0.77 (4.96)**	**1.06 (2.40)**	**0.70 (2.84)**	**0.89 (0.97)**	**0.69 (1.58)**

For infinite wedges, calculating transfer functions at 30 frequencies took approximately half the time required for UTD with the approximation proposed by [10]. Calculating the IIR filter parameters took a similar computation time. For finite wedges, the computation with UDFA took approx. twice as long as for infinite wedges with UDFA, and therefore was comparable to UTD, which is only applicable for infinite wedges. Accordingly, for finite wedges, a comparison can only be performed to BTMS, which is not feasible for real-time applications and orders of magnitude slower (see also [27]). Thus, for finite wedges, the extensions of UDFA presented here constitute the only physics-based approach applicable for real time applications.

Extending the runtime evaluation of the underlying approach in [27], for the filter design, and parameter estimation as well as for running the filters, the required floating point operations (FLOPs) per sample can be estimated:

i) Computational filter running costs: Depending on the level of accuracy chosen for the IIR implementation, 1–8 second-order-section (SOS) filters are used per diffraction path across a finite or infinite wedge. At runtime, each SOS requires 9 FLOPs per sample, identical to the description in [28]. For further runtime comparisons and considerations of the filter running costs, see [28]. Additional filters are required for the heuristic HO approximation described in Section 3.2, where the second-order Linkwitz-Riley cascade is computationally very efficient during filter design and runtime.

For diffraction at a three-sided barrier, in addition to the two diffraction filters that are required for a sequential diffraction, two additional (single-term) filters are required for the (more accurate) approximation suggested here. Thereby, an increase of overall filter running cost by approximately 50% is traded off for substantially increased accuracy.

ii) Parameter calculation costs: The costs of our filter parameter calculation depend on the particular implementation and its respective design choices: We estimate that for the calculation of IIR filter coefficients from geometrical parameters (vectors describing the position of source, edge, and receiver), in the simplest case 112 FLOPs are required to generate a 1 SOS filter representation. At runtime, these operations are required for each parameter update (e.g., at 60 frames per second). For an infinite wedge, using the two-term solution, and using a pair of 2 SOS filters, 394 FLOPs are required. For the (high-precision approximation) of a finite wedge, composed of two half-wedges each represented with a pair of 2 SOS filters, 848 FLOPs are required. These numbers can be compared to estimated parameter calculation cost for the machine learning approach in [33], which amount to 9786 and 1976 FLOPs per diffraction order (wedge) for their best and fast neural net, respectively.

For the finite-wedge filter parameters of the current approach, a few of the required operations are more complex, e.g., the atan (Eq. (10), [27]). Here, a series evaluation could be terminated after a small number of terms or a lookup table would be sufficient. Moreover, evaluating the target filter function (Eqs. 20 and 21, [26]) as required for the filter design contributes significantly to the computational costs

and involves non-integer exponential functions. However, this part can be completely replaced by a lookup table (given that only the cutoff frequency of the same underlying filter function changes). By this, the above estimated FLOPs for the parameter estimation can be reduced by at least 20%.

5 Discussion

5.1 Physically-based and data-driven diffraction approaches

This paper describes physically-based diffraction filter approximations with low computational complexity, suited for interactive VA applications. The required diffraction paths can be determined by pathfinding algorithms, e.g., [4] and [5]. Besides pathfinding, determining and implementing the spectral content of diffraction paths in a computationally efficient manner has so far posed a challenge, particularly for finite objects and the underlying finite wedges. Previous filter approaches, recursive [3] and finite-impulse response filters [24, 35], were still based on integral expressions [9, 15], and thus provided limited improvements of computational efficiency. UDFA, underlying the approaches suggested here, parametrizes the diffracted sound by filter cutoff frequencies and gains, derived from the geometrical parameters, and can thus be implemented very efficiently.

Other recent approaches to integrating diffraction in VA are data-driven. Mannall et al. [28] presented a machine learning approach to obtain recursive filters for edge diffraction in the shadow zone, for diffraction of single and consecutive wedges. They compare their spectral accuracy to BTMS and our earlier heuristic filter-approximation for the shadow zone [25]. Their restriction to rendering diffraction in the (double) shadow zone limits the applicability for smooth transitions around entire objects. Also, their sequential approach for diffraction at consecutive wedges disregards the effect of the second edge in the single VZ, while the current approach uses a modified exterior wedge angle. The current evaluation in the DSZ showed that sequential approaches successfully approximate the asymptotic high-frequency behavior for widely (far-field) spaced double edges, as here exemplified by the 10 m double edge width. High-frequency errors increase for smaller edge widths and considerable low-frequency errors occur independent of edge width.

Regarding the computational complexity of different configurations of the here extended UDFA and the approach from [28], the underlying recursive filters use exactly the same number of floating point operations (FLOPs) for the single-SOS approximation of UDFA. The here proposed double edge approximation requires more filters (while offering a wider applicability). The computation of the filter coefficients for finite and infinite single wedges is considerably faster (and exact) using the physics-based UDFA approach, estimated at about 150–1000 FLOPs depending on edge geometry and filter order, in comparison to about 2000 or 10,000 FLOPs for different model precisions in [28].

Machine learning has also been applied to describe diffraction from objects [31–34]. Such approaches can be highly computationally efficient for three-dimensional objects that consist of many edges or are spherical. Another advantage is that effects of higher-order diffraction from objects can be included in the data-driven model. However, the abstraction from edges to objects tends to reduce the level of detail in rendering. This is observable in the above-mentioned publications as a reduced representation of spectral fine structure. It is conceivable that data-driven, object-based approaches and edge-diffraction-based rendering could be combined in a rendering framework with multiple levels of acoustic detail.

In contrast to data-driven approaches, the current approach, despite its efficiency, still offers a physically-interpretable solution and a physically-motivated filter architecture for objects. Given the scalable accuracy of the underlying UDFA solution or the general filter representation of diffraction in [26], implementations of the current approach can be adapted to make use of available computational resources or meet the precision requirements of highly detailed room acoustic simulation and noise prediction.

5.2 Diffraction at flat objects and the heuristic higher-order extension

One challenge for existing diffraction approaches in the framework of GA is a smooth sound field. Flat objects cover important classes of objects in virtual acoustic environments (screens, tabletops). The proposed approach of modeling first-order diffraction from a flat finite object by superimposing the contributions from its finite edges using UDFA has been successfully applied in a study on binaural perception [30], where in comparison to measured impulse responses, a high level of agreement could be achieved, both on a technical and perceptual level. Another previous approach to binaurally render the sound field around a computer-screen sized object was described by Pulkki and Svensson [31], based on machine-learning derived recursive filters. In the context of their perceptual evaluation, where the virtual listeners were moved around the object, degraded ratings for some of their tested methods were associated with rapid spectral changes, underlining the important role of spatial smoothness. The current contribution provides a filter topology applicable for single edges and objects to provide smooth transitions.

For flat objects, composed of several (knife) edges, complementary low- and high-pass filters were suggested to heuristically approximate the spectral effects of HO diffraction and at the same time to ensure a smooth sound field around the entire object. To the authors' knowledge, the current approximation constitutes the only published real-time feasible approach providing both, a smooth sound field and the spectral fine structure which can be attributed to the different travel paths around each edge of an object. Other approaches reduce diffraction rendering around an object to only a single path [5] and/or rely on further simplifications to determine their spectral content [32].

The approach suggested here can straightforwardly be incorporated into typical GA-based rendering systems and can also be adapted to openings in flat surfaces. Reflections, including HO diffraction effects from finite objects are modeled by the high-pass part of the suggested crossover filter structure. The proposed cross-over topology can also be adapted to account for spectral effects of HO diffraction from three-dimensional objects in the frequency range with wavelengths larger than the object dimensions.

5.3 Double diffraction and three-dimensional objects

In strongly reverberant indoor environments, some of the discontinuities for moving sources or receivers resulting from GA rendering without diffraction might have a weaker perceptual impact. However, in outdoor environments, a sound source that abruptly becomes audible when, e.g., passing a corner would be highly unrealistic. For such scenarios, three dimensional objects and diffraction at consecutive edges along a path are important. The current study focused on the three-sided barrier, which can be considered as a simplification of long buildings or as a prototype for constructing double diffracted paths around three-dimensional objects.

In contrast to earlier asymptotic solutions [8, 10, 22], the current approach simplified the problem to two edge contributions in the double SZ and the double VZ, where both source and receiver are above the top plane of the barrier, and to the singly-diffracted field (using a modified exterior edge angle) otherwise. Deviations in the tested scenarios were generally small, and so far, no other methods exist that are physically-based, computationally efficient, and take into account spatial smoothness. Extending the concept of the flat plate, diffraction for arbitrary cube objects or even more complicated three-dimensional structures could be composed of multiple double (and single) diffracted paths.

The current double edge solution has, however, some limitations which should be mentioned. Transitions at the RSB were not considered here: i) For small d_w, the modification of the exterior wedge angles (for providing a transition towards $d_w = 0$) results in wrong locations of the RSB in the view zone. It would thus be recommended to not simulate geometric reflections from the small surface between the two edges, which would be limited to high frequencies for small d_w anyway (see Sect. 3.2). ii) For large d_w, the modification of the exterior wedge angles could be omitted to obtain the correct locations of the RSB in the view zone.

Generally, regarding future extensions to multiple diffracting edges, using a diffraction path which connects the source via the apex point to the listener simplifies the diffracting edge to a point source. The underlying line source properties of the diffracting edge (see also [44]) are contained in the diffraction impulse response for the diffraction path. However, diffracted sound that is transmitted from the edge into directions other than the listener's direction is ignored by this path-based representation. Nevertheless, for double diffraction, this path-based description has led to good agreement with the reference. Likewise, it is possible to approximate consecutive diffraction at multiple wedges on different objects by using the direction of the apex point of previous and subsequent wedges to determine the source and receiver position for the sequential diffraction instances [23, 28, 35]. However, the error evaluation in Section 3.3.3 revealed a benefit of the approximation proposed here, compared to the sequential approximation using the extension method proposed in [28]. Errors of the sequential approximation for the three-sided barrier might be reduced by using the apex points on the adjacent edge for constructing diffraction paths, reflecting a further simplification of the method. For future research, investigations are required regarding the approximation of diffraction from subsequent non-parallel edges or in conditions with only partial visibility of the edges.

6 Conclusion

Computationally-efficient approaches to modeling edge diffraction are essential for interactive real-time auralization of indoor and outdoor environments. Here, an existing filter-based approach to diffraction modeling has been extended to approximate spectral effects of higher-order (HO) diffraction, which is a key phenomenon to achieve a spatially smooth sound field around diffracting objects in VA. Spatial smoothness has been investigated and the current extensions and techniques have been shown to accurately approximate HO diffraction at finite flat objects and a three-sided barrier:

- A filter topology for rendering filter-based diffraction paths in the context of GA was suggested, providing a spatially smooth sound field for infinite wedges and for finite objects.
- Spectral effects of HO diffraction can be approximated using an additional crossover filter structure, where edge diffraction is only considered in the high-pass path representing large object dimensions in relation to the wavelength of the sound. The suggested method also reproduces high-pass reflections from finite objects.
- Diffraction at a three-sided barrier can be well approximated using diffraction filters with smooth transitions from a 6-dB/oct slope in the double diffracted case to a 3-dB/oct slope when the single-diffracted field dominates. The suggested solution provides the basis for efficient simulation of diffraction around three-dimensional objects.

Funding

This work was funded by the Deutsche Forschungsgemeinschaft, DFG – Project-ID 352015383 – SFB 1330 C5.

Conflicts of interest

The authors have no competing interests to declare that are relevant to the content of this article.

Data availability statement

The simulated data are available from the corresponding author on request. The underlying methods for the simulations are available as part of the UDFA toolbox [38].

References

1. R. Torres, M. Kleiner, B.-I. Dalenbäck: Audibility of "diffusion in room acoustics auralization: an initial investigation, Acta Acustica united with Acustica 86, 6 (2000) 919–927.
2. R.R. Torres, U.P. Svensson, M. Kleiner: Computation of edge diffraction for more accurate room acoustics auralization, Journal of the Acoustical Society of America 109, 2 (2001) 600–610. https://doi.org/10.1121/1.1340647.
3. T. Lokki, U.P. Svensson, L. Savioja: An efficient auralization of edge diffraction, in: AES 21st International Conference, St. Petersburg, Russia, 1–3 June, 2002.
4. A. Erraji, J. Stienen, M. Vorländer: The image edge model, Acta Acustica 5 (2021) 17. https://doi.org/10.1051/aacus/2021010.
5. C. Schissler, G. Mückl, P. Calamia: Fast diffraction pathfinding for dynamic sound propagation, ACM Transactions on Graphics 40, 4 (2021) 1–13. https://doi.org/10.1145/3450626.3459751.
6. J.B. Keller: Geometrical theory of diffraction, Journal of the Optical Society of America 52, 2 (1962) 116–130. https://doi.org/10.1364/JOSA.52.000116.
7. M.A. Biot, I. Tolstoy: Formulation of wave propagation in infinite media by normal coordinates with an application to diffraction, Journal of the Acoustical Society of America 29, 3 (1957) 381–391. https://doi.org/10.1121/1.1908899.
8. A.D. Pierce: Diffraction of sound around corners and over wide barriers, Journal of the Acoustical Society of America 55, 5 (1974) 941–955. https://doi.org/10.1121/1.1914668.
9. R.G. Kouyoumjian, P.H. Pathak: A uniform geometrical theory of diffraction for an edge in a perfectly conducting surface, Proceedings of the IEEE 62, 11 (1974) 1448–1461. https://doi.org/10.1109/PROC.1974.9651.
10. T. Kawai: Sound diffraction by a many-sided barrier or pillar, Journal of Sound and Vibration 79, 2 (1981) 229–242. https://doi.org/10.1016/0022-460X(81)90370-9.
11. T. Funkhouser, N. Tsingos, I. Carlbom, G. Elko, M. Sondhi, J.E. West, G. Pingali, P. Min, A. Ngan: A beam tracing method for interactive architectural acoustics, Journal of the Acoustical Society of America 115, 2 (2004) 739–756. https://doi.org/10.1121/1.1641020.
12. C. Schissler, R. Mehra, D. Manocha: High-order diffraction and diffuse reflections for interactive sound propagation in large environments, ACM Transactions on Graphics 33, 4 (2014) 1–12. https://doi.org/10.1145/2601097.2601216.
13. N. Tsingos, T. Funkhouser, A. Ngan, I. Carlbom: Modeling acoustics in virtual environments using the uniform theory of diffraction, in: Proceedings of the 28th Annual Conference on Computer Graphics and Interactive Techniques – SIGGRAPH '01, ACM Press, New York, NY, USA, 2001, pp. 545–552. https://doi.org/10.1145/383259.383323.
14. H. Medwin: Shadowing by finite noise barriers, Journal of the Acoustical Society of America 69, 4 (1981) 1060–1064. https://doi.org/10.1121/1.385684.
15. U.P. Svensson, R.I. Fred, J. Vanderkooy: An analytic secondary source model of edge diffraction impulse responses, Journal of the Acoustical Society of America 106, 5 (1999) 2331–2344. https://doi.org/10.1121/1.428071.
16. U.P. Svensson, P.T. Calamia, S. Nakanishi: Frequency-domain edge diffraction for finite and infinite edges, Acta Acustica united with Acustica 95, 3 (2009) 568–572. https://doi.org/10.3813/AAA.918181.
17. A. Asheim, U.P. Svensson: Efficient evaluation of edge diffraction integrals using the numerical method of steepest descent, Journal of the Acoustical Society of America 128, 4 (2010), 1590–1597. https://doi.org/10.1121/1.3479545.
18. R. Torres, N. Rycker, M. Kleiner: Edge diffraction and surface scattering in concert halls: physical and perceptual aspects, Journal of Temporal Design in Architecture and the Environment 4 (2004) 52–58.
19. U.P. Svensson, S.R. Martin, J. Šlechta, J.E. Summers, B.H. Teres, C.F. Gaumond: Accuracy aspects for diffraction-based computation of scattering, in: Proceedings of the Euronoise 2018 Crete, Heraklion, Crete, Greece, 27–31 May, European Acoustics Association, 2018, pp. 2093–2098.
20. J. Rindel: Attenuation of sound reflections due to diffraction, in: Nordic Acoustical Meeting, Aalborg, Denmark, 20–22 August, 1986.
21. J.H. Rindel: Acoustic design of reflectors in auditoria, Proceedings of the Institute of Acoustics 14, 2 (1992) 119–129.
22. D. Chu, T.K. Stanton, A.D. Pierce: Higher-order acoustic diffraction by edges of finite thickness, Journal of the Acoustical Society of America 122, 6 (2007) 3177–3194. https://doi.org/10.1121/1.2783001.
23. H.-S. Kim, J.-S. Kim, H.-J. Kang, B.-K. Kim, S.-R. Kim: Sound diffraction by multiple wedges and thin screens, Applied Acoustics 66, 9 (2005) 1102–1119. https://doi.org/10.1016/j.apacoust.2005.01.004.
24. P.T. Calamia, U.P. Svensson: Fast time-domain edge-diffraction calculations for interactive acoustic simulations, EURASIP Journal on Advances in Signal Processing 2007, 1 (2006) 1. https://doi.org/10.1155/2007/63560.
25. C. Kirsch, S.D. Ewert: Low-order filter approximation of diffraction for virtual acoustics, 2021 IEEE Workshop on Applications of Signal Processing to Audio and Acoustics (WASPAA), IEEE, New Paltz, NY, USA, 2021, pp. 341–345. https://doi.org/10.1109/WASPAA52581.2021.9632674.
26. S.D. Ewert: A filter representation of diffraction at infinite and finite wedges, JASA Express Letters 2, 9 (2022) 092401. https://doi.org/10.1121/10.0013686.
27. C. Kirsch, S.D. Ewert: A universal filter approximation of edge diffraction for geometrical acoustics, IEEE/ACM Transactions on Audio, Speech, and Language Processing 31 (2023) 1636–1651. https://doi.org/10.1109/TASLP.2023.3264737.
28. J. Mannall, L. Savioja, P. Calamia, R. Mason, E. De Sena: Efficient diffraction modeling using neural networks and infinite impulse response filters, Journal of the Audio Engineering Society 71, 9 (2023) 566–576.
29. C. Kirsch, S.D. Ewert: Filter-based first- and higher-order diffraction rendering, in: Proceedings of the 10th Convention of the European Acoustics Association, Turin, Italy, 11–15 September, 2023, Politecnico di Torino, Torino, Italy, pp. 6181–6187. https://doi.org/10.61782/fa.2023.1128.
30. C. Kirsch, S.D. Ewert: Effects of measured and simulated diffraction from a plate on sound source localization, Journal of the Acoustical Society of America 155, 5 (2024) 3118–3131. https://doi.org/10.1121/10.0025922.
31. V. Pulkki, U.P. Svensson: Machine-learning-based estimation and rendering of scattering in virtual reality, Journal of the Acoustical Society of America 145, 4 (2019) 2664–2676. https://doi.org/10.1121/1.5095875.

32. L. Pisha, S. Atre, J. Burnett, S. Yadegari: Approximate diffraction modeling for real-time sound propagation simulation, Journal of the Acoustical Society of America 148, 4 (2020) 1922–1933. https://doi.org/10.1121/10.0002115.
33. S. Wirler, S.J. Schlecht, V. Pulkki: Machine learning based auralization of rigid sphere scattering, in: 2021 Immersive and 3D Audio: from Architecture to Automotive (I3DA), Bologna, Italy, 8–10 September, IEEE, 2021, pp. 1–8. https://doi.org/10.1109/I3DA48870.2021.9610951.
34. L. Pisha, S. Yadegari: Specular path generation and near-reflective diffraction in interactive acoustical simulations, IEEE Transactions on Visualization and Computer Graphics 30, 7 (2023) 3609–3621. https://doi.org/10.1109/TVCG.2023.3238662.
35. D. Schröder: Physically based real-time auralization of interactive virtual environments, Dissertation, 2011, RWTH Aachen, Logos Verlag, Berlin.
36. J. Vanderkooy: A simple theory of cabinet edge diffraction, Journal of the Audio Engineering Society 39, 12 (1990) 923–933.
37. U.P. Svensson: ED toolbox, v 0.504. [Online]. Available at https://github.com/upsvensson/Edge-diffraction-Matlab-toolbox.
38. Kirsch C., Ewert S.D.: Universal diffraction filter approximation (UDFA) Toolbox for Mathwork's MATLAB Zotero, 2024. https://doi.org/10.5281/zenodo.13771101
39. T.W. Veruttipong: Time domain version of the uniform GTD, IEEE Transactions on Antennas and Propagation 38, 11 (1990) 1757–1764. https://doi.org/10.1109/8.102736.
40. P.R. Rousseau, P.H. Pathak: TD-UTD for scattering from a smooth convex surface, IEEE Antennas and Propagation Society International Symposium. 1996 Digest 3 (1996) 2084–2087. https://doi.org/10.1109/APS.1996.550019.
41. R. Bücklein: Hörbarkeit von Unregelmäßigkeiten in Frequenzgängen bei akustischer Übertragung (detection of irregularities in the frequency responses of acoustic transmissions), in: Elektroakustik II. Nachrichtentechnische Fachberichte, 26, J. Wosnik (Ed.), Vieweg Teubner Verlag, Wiesbaden, Germany, 1962, pp. 42–47.
42. B.C.J. Moore, C.-T. Tan: Perceived naturalness of spectrally distorted speech and music, Journal of the Acoustical Society of America 114, 1 (2003) 408–419.
43. J. Mannall, O. Das, P. Calamia, E. De Sena: Perceptual evaluation of low-complexity diffraction models from a single edge, in: Audio Engineering Society Conference: AES 2022 International Audio for Virtual and Augmented Reality Conference, Redmond, WA, USA, 15–17 August, Audio Engineering Society, 2022, pp. 1–10.
44. V. Pulkki, T. Lokki: Visualization of edge diffraction, Acoustics Research Letters Online 4, 4 (2003) 118–123. https://doi.org/10.1121/1.1605131.

Cite this article as: Kirsch C. & Ewert SD. 2024. Filter-based first- and higher-order diffraction modeling for geometrical acoustics. Acta Acustica, **8**, 73. https://doi.org/10.1051/aacus/2024059.

Appendix

For approximating the three-sided barrier with a single diffracting wedge, the low-frequency effect of the second edge can be accounted for by the ratio of the exterior wedge angle of the single edge and the total exterior wedge angle, resulting in the DC gain $g_{\mathrm{DC1,2}} = \hat{\theta}_{\mathrm{w1,2}}/(\theta_{w1} + \theta_{w2} - \pi)$ for either edge. This relation reflects that at DC, the sound field covers the total exterior wedge angle, while the diffraction function assumes the smaller exterior wedge angle $\hat{\theta}_{\mathrm{w1,2}}$. The filter gain calculated with equation (3) is now multiplied with $g_{\mathrm{DC1,2}}$ and the filter cutoff frequency (Eq. (1)) is modified to maintain the asymptotic high-frequency behavior, $f_{\mathrm{c,mod}} = f_{\mathrm{c}}/g_{\mathrm{DC}}^2$ (see [27]). These modifications are applied to the two filters of the diffraction function using weighted gains based on the cut off frequency ratio with $g_{\mathrm{DC}+,-} = g_{\mathrm{DC}}/(1 + \sqrt{f_{\mathrm{c}+,-}/f_{-,+}})$ for either edge, ensuring a stronger modification of the filter with the lower cutoff frequency.